Spatial Coherence of Speckle for Repeat-Pass Synthetic Aperture Sonar Micronavigation

Stig Asle Vaksvik Synnes, *Member, IEEE*, Roy Edgar Hansen, *Senior Member, IEEE*,
and Torstein Olsmo Sæbø, *Senior Member, IEEE*

***Abstract*—Accurate positioning of autonomous underwater vehicles is a major challenge. The long-term drift is problematic if global position updates are not available, and for applications such as repeat-pass interferometry and coherent change detection, millimeter accuracy is needed. Repeat-pass synthetic aperture sonar (SAS) micronavigation is one potential technique for countering both challenges. While single-pass SAS micronavigation enabled successful coherent processing within one track, the potential is that repeat-pass SAS micronavigation can support coherent processing between passes. Both techniques are based on recognizing the speckle pattern in the seafloor return, but repeat-pass SAS micronavigation has additional challenges with the larger temporal and spatial separations between the observations. In this study, we investigate the spatial correlation of speckle as observed from SAS systems. We divide the different contributions to spatial decorrelation into three groups: 1) speckle decorrelation; 2) footprint mismatch; and 3) stretching. We examine each contribution separately and develop simplified formulas for their decorrelation baselines. When correlating synthetic aperture images, decorrelation from stretching dominates. When correlating single-element data recorded at low grazing angles common to SAS, speckle decorrelation dominates. We validate our findings on experimental data, and by combining elements into larger effective elements, we demonstrate increasing the across-track baseline for repeat-pass SAS micronavigation updates from less than 1 to 10 m.**

***Index Terms*—Interferometry, navigation, spatial coherence, synthetic aperture sonar (SAS).**

I. INTRODUCTION

AUTONOMOUS underwater vehicles (AUVs) with synthetic aperture sonar (SAS) are used for a wide range of applications, including search and survey [1], marine geology [2], habitat monitoring [3], environmental monitoring [4], naval mine countermeasures [5], change detection [6], [7], and underwater archeology [8], and there is a huge potential of using SAS for bathymetric mapping [9], [10]. Many of these applications pose challenging demands for the AUV navigation, both regarding short-time position accuracy and long-term drift. A range of techniques are available both for absolute and relative position updates [11]. Absolute position updates can be obtained from global navigation satellite systems, either by relaying position updates from a surface vessel or through surfacing. However, operating a surface vessel can be costly, and surfacing the underwater vehicle is not practical for operations at large depth or in highly trafficked areas. The use of terrain navigation with premade maps is a well-demonstrated alternative for acquiring absolute or relative navigation updates in the underwater domain [12], [13]. While this technique exploits terrain variations, its companion technique of feature-based navigation can operate on smaller features or objects. Correlation of images can also be used for navigation, supporting distributed features or feature-points in intensity images [14], [15], or even direct correlation of image snippets using either intensity data or complex data [7], [16]. Furthermore, successful SAS image formation is usually only obtained after incorporating micronavigation updates from the SAS sensor into the vehicle navigation [17]. Initial studies have demonstrated that SAS micronavigation measurements can be used to obtain navigation updates also between passes under controlled experimental setups [18]–[20].

A. Repeat-Pass SAS Micronavigation

Acoustic measurements on the seafloor typically return a speckle intensity pattern, originating from the superimposed backscattering of randomly distributed scatterers within each resolution cell [21, Ch. 4.3]. If the relative distance to the individual scatterers changes, the speckle pattern also changes. SAS micronavigation is based on recognizing the speckle pattern between time series of acoustic backscatter. Using a SAS system with a multielement receiver array, element data of partially overlapping array positions from consecutive pings are crosscorrelated in a search for the element pair and relative time delay with the highest degree of coherence, and the corresponding arguments give the along-track displacement and slant-range displacements [17], [22], [23].

Successful correlation of sensor data between passes is limited by temporal decorrelation, the relative orientation of the tracks, and the spatial separation between tracks [24]. Temporal decorrelation periods for the seafloor vary from days to perhaps a month in coastal shallow water at 100 kHz, but

---

Manuscript received December 13, 2019; revised August 28, 2020, January 5, 2021, and February 5, 2021; accepted February 15, 2021. Date of publication May 31, 2021; date of current version October 13, 2021. This work was supported by The Norwegian Defence Research Establishement and Kongsberg Maritime. *(Corresponding author: Stig Asle Vaksvik Synnes.)*

Associate Editor: M. Hayes.

Stig Asle Vaksvik Synnes and Roy Edgar Hansen are with the Defence Systems Division, Norwegian Defence Research Establishment (FFI), N-2027 Kjeller, Norway, and also with the Department of Informatics, University of Oslo (UiO), N-0316 Oslo, Norway (e-mail: Stig-Asle.Synnes@ffi.no; roy-edgar.hansen@ffi.no).

Torstein Olsmo Sæbø is with the Defence Systems Division, Norwegian Defence Research Establishment (FFI), N-2027 Kjeller, Norway (e-mail: torstein-olsmo.sabo@ffi.no).

Digital Object Identifier 10.1109/JOE.2021.3060812

will be significantly shorter at higher frequencies, in rough weather, with strong currents, or with high animal activity at the seafloor [6], [25], [26]. Decorrelation from relative orientation between tracks was derived in [24] and measured in [20]. Its impact can be minimized by minimizing the relative orientation of the tracks, and potentially also through beamsteering. The decorrelation with across-track separation has been visited only in preliminary studies, demonstrating valid repeat-pass micronavigation measurements for across-track separations of up to 0.7 m [18], [19]. A potential applicability to significantly longer separations has been indicated [18]. With a larger tolerance to across-track separation, navigation updates can also be acquired after a larger drift from the original position. Thus, the tolerance to across-track separation constitutes a key parameter for the feasibility of repeat-pass SAS micronavigation updates [16].

In this article, we perform an in-depth study of the limitations to spatial separation for successful repeat-pass SAS micronavigation. Initially, we review the current status on estimation of the spatial coherence.

B. Spatial Coherence

The similarity of the speckle pattern between two recordings of acoustic backscatter can be expressed by the degree of coherence. The correlation function—or the spatial variance of the coherence—for an aperture is predicted from the van Cittert–Zernike theorem. This theorem has been successfully applied to optics and radio astronomy, and also to pulsed echo ultrasound [27, Ch. 10.4.2.a], [28, Ch. 15], [29].

The decorrelation with *along-track baseline* is used for motion estimation in correlation sonar, including SAS micronavigation. Accurate knowledge of its functional form is crucial for acquiring navigation estimates of high accuracy and low bias [17], [22], [23], [30, Ch. 5], [31].

The decorrelation with *range baseline* is fundamental for the applicability of SAS data from repeated passes. However, we have been unable to locate any prior study on the range baseline. We, therefore, evaluate the van Cittert–Zernike theorem for this dimension, and also derive simplified expressions on the feasible baselines for both along-track and range correlation.

The decorrelation with a *change of grazing angle* between observations has been studied for the application of repeat-pass SAR interferometry. Using an approach in line with the van Cittert–Zernike theorem, the decorrelation was first derived for an idealized geometry and shortly thereafter for more realistic scattering surfaces and interferometer geometries [24], [32], [33]. This decorrelation was later related to the ground wave number mismatch originating from a relative stretch between the observations [34], [35].

We find it useful to group the different contributions to decorrelation into the three groups of 1) *footprint mismatch*, addressing decorrelation from different illumination of the scene; 2) *speckle decorrelation*, addressing decorrelation caused by different coherent contributions from scatterers within each range sample; and 3) *stretching*, addressing decorrelation from different coherent contribution between range samples. We recognize that decorrelation by footprint mismatch can be reduced by beamsteering and beamforming, and decorrelation from stretching can be reduced by destretching the time series. In contrast, speckle decorrelation is fundamental and cannot be avoided.

C. Claim

We investigate the spatial coherence of speckle for repeat-pass SAS micronavigation. In particular, the following statements hold.

1) We derive *simple formulas* for the baseline decorrelation for each of the contributions to spatial decorrelation.
2) We show that *speckle decorrelation* with range baseline constitutes the most prominent source of decorrelation for single elements at small grazing angles.
3) We show that when combining elements into practical synthetic aperture lengths, decorrelation from *wave number stretching* constitutes the most prominent source of decorrelation if the stretching is left uncompensated.
4) We show how decorrelation from wave number stretching dominates over *wave number mismatch*, for the case of uncompensated stretching when using the same frequency band for both observations.
5) We estimate a *coherence floor*, or lower limit on the expectation value, for estimating coherence values through crosscorrelation.
6) We demonstrate good *agreement* of spatial decorrelation estimates from the theoretical predictions, our simplified formulas, and the experimental results.
7) We demonstrate *an increase of* the across-track baseline of successful repeat-pass SAS micronavigation updates from the less than 1 m reported in [18] and [19] to more than 10 m.

D. Outline

In Section II, we introduce the system geometry of interferometric SAS and the estimation of spatial coherence, including our derivation of the coherence floor. We evaluate the theoretical limit on the spatial coherence from the van Cittert–Zernike theorem, and derive simplified formulas for the maximum feasible along-track and range baselines limited by speckle decorrelation in Section III. In Section IV, we evaluate the decorrelation by footprint mismatch, and in Section V, we evaluate the decorrelation from a change of grazing angle, expressed as a relative stretching of the ground wave number spectrum. We estimate both the decorrelation without destretching, and we quantify the remaining effect of wave number mismatch after a presumed ideal destretching. In Section VI, we assemble our predictions in a table of simplified formulas for decorrelation baselines of coherence 0.5 for each of the investigated sources of decorrelation. We validate our findings on SAS measurements from an operational AUV in Section VII. In Section VIII, we examine both our theoretical predictions and our measurement results. Finally, we summarize our main findings in Section IX.

II. SPATIAL COHERENCE ESTIMATION

In this section, we present the geometry of interferometric SAS system and micronavigation measurements, before we

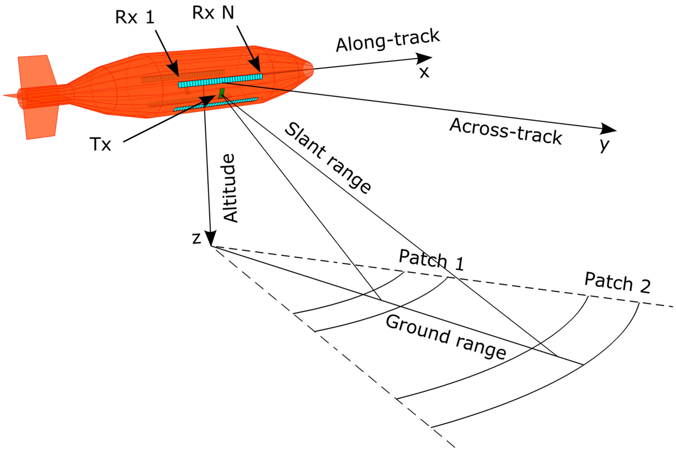

Fig. 1. Observation geometry of an interferometric SAS system, together with the acoustic footprint on the seafloor and relevant coordinate systems.

give a brief introduction to the estimation of spatial coherence through cross correlation of time series. We contribute by evaluating the effective coherence floor (or bias) on the expectation value of the maximum degree of coherence from a cross correlation.

A. System Geometry

SAS processing is based on combining data from multiple pings to synthesize long apertures, allowing for generation of high-resolution images also at long range. SAS systems also employ multielement receiver arrays, allowing them to transit further between pings, thereby increasing the area coverage rate [36].

Fig. 1 shows the measurement geometry of an interferometric SAS system on an AUV with one transmitter and two vertically displaced receiver arrays. Using an interferometric SAS additionally allows for estimating the seafloor bathymetry [37]. We have indicated the relevant local earth-fixed coordinate system [x, y, z] that represents the along-track and across-track positions, and the altitude. The SAS system insonifies the seafloor within the sonar beamwidth, and we illustrate two range-patches through their seafloor footprint. The sonar data are recorded as a function of time and thereby, correspond to the slant-range representation. The footprint of a patch on the seafloor constitutes the ground range representation.

B. Phase Center Approximation

The use of multielement receiver arrays and a moving AUV platform leads to a bistatic recording geometry, with the transmitter in one focal point, and each receiver in the other. This geometry can be simplified by representing each pair by an effective monostatic element at the phase center between the transmitter and each receiver. This approximation is valid for ranges $r \gg D^2/4\lambda$, where D is the distance between the transmitter and receiver positions and λ is the wavelength at the center frequency [17]. Throughout this article, we adopt the phase center approximation (PCA), and obtain an array of PCA-elements with half the effective element spacing of the physical receiver element spacing.

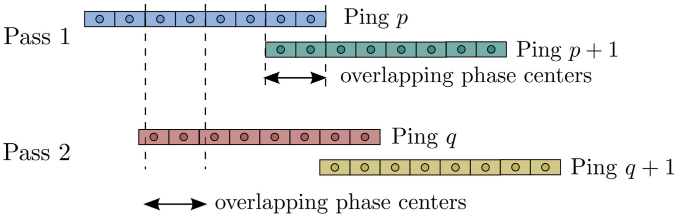

Fig. 2. Overlapping phase centers between consecutive pings p and $p+1$ from pass 1, and between ping p from pass 1 and ping q from pass 2. For the latter case, we indicate only two out of many overlapping phase centers.

C. SAS Micronavigation

The SAS system transmits an acoustic signal into the water. The signal is scattered back by the seafloor and is observed by the receiver array. The receiver elements make spatially independent observations of the *scattered field*. Element data from different pings, recorded at roughly the same position, can be correlated to provide navigation updates. Overlapping phase centers will have the highest coherence, and give the along track displacement, while the relative change in round trip time gives the slant-range displacement [17], [22], [23]. The accuracy of the estimates follows from the degree of coherence and the system parameters [17]. Revisiting a phase center position between consecutive pings in a pass can be achieved by operating with overlapping phase centers in the technique of micronavigation [17], and between passes by rerunning a pass at a small crossing angle [18]. The resulting element combinations are illustrated in Fig. 2.

D. Signal Model

Assume a scene containing a random distribution of scatterers that are small compared to a resolution cell. This results in a speckle scene, and the pixel values possesses a circularly symmetric complex Gaussian distribution [21, Ch. 4.3]. We assume that the noise is additive and white and, thus, also possesses a circularly symmetric complex Gaussian distribution.

We model the data $a_i(t)$, recorded as a function of ping propagation time t from two repeated passes $i \in \{1, 2\}$ over a scene, as the combination of one common signal component $g(t)$, with amplitude s, and a random noise realization $h_i(t)$, with amplitude n

$$\begin{aligned} a_1(t) &= sg(t) + nh_1(t) \\ a_2(t, \tau_0) &= sg(t - \tau_0) + nh_2(t) \end{aligned} \tag{1}$$

where τ_0 is an unknown relative delay of signal 2.

E. Degree of Coherence

We choose to express the similarity between the two signals a_1 and a_2 through their *degree of coherence* γ, representing their linear dependence versus time delay τ between the signals

$$\hat{\gamma}(\tau) = \frac{|\langle a_1^*(t) a_2(t-\tau)\rangle|}{[\langle |a_1(t)|^2\rangle \langle |a_2(t)|^2\rangle]^{1/2}}. \tag{2}$$

Here, $\hat{}$ indicates an estimate, * represents the complex conjugate, and $\langle\,\rangle$ is an ensemble over time. By insertion of (1) into (2) and accounting for the delay by setting $\tau = \tau_0$, it follows that if the noise components are independent both of each other and of the signal, the population coherence directly relates to the signal energy s^2 and the noise energy n^2 [24]

$$\gamma = \frac{s^2}{s^2 + n^2}. \tag{3}$$

For *finite-time series*, the assumptions of independence between the time series do not hold, and the coherence estimator of (2) will have a bias toward higher values. This bias is most prominent for lower coherence values and few independent samples, as derived from the probability density function $p(\hat{\gamma}|\gamma, M)$ of the coherence estimate $\hat{\gamma}$, which is available as a function of population coherence γ and a number of independent samples M in [38].

F. Cross Correlation

An unknown time delay between two complex time series can be estimated by cross correlation, evaluating the degree of coherence from (2) for a range of candidate delays, and choosing the delay corresponding to the maximum degree of coherence. However, in the case of finite-length uncorrelated sequences, selecting the maximum value over many delays causes an increase in the maximum value. This again, causes an increased bias in the estimated coherence. We find that in-depth knowledge of this bias is important for choosing a good implementation of the time-delay estimation. In the remainder of this section, we derive this bias, and compute the resulting coherence floor.

1) Bias: We choose a cross-correlation implementation that estimates the coherence over all candidate lags using a sliding window inner product. Thus, we avoid any bias (or weighting) from nonoverlapping time series for nonzero lags. Next, we assume that the signals are critically sampled and estimate the coherence for lags corresponding to L different sample offsets. Thus, all except one of the lags should correspond to correlating noise with noise. Their expected maximum value will increase with the number of lags evaluated, and constitutes a bias on the cross-correlation estimate. Such a bias can be expressed as

$$b = E\{\hat{x}\} - x \tag{4}$$

where $\hat{x}$ is the estimated value and x the true value. For a distribution with nonzero probability of estimates $\hat{x} > 0$ only, the expected value can be calculated directly from the cumulative distribution function (cdf) $P(\hat{x})$ [39, p. 29]

$$E\{\hat{x}\} = \int_0^\infty (1 - P(\hat{x}))\, d\hat{x}. \tag{5}$$

The criterion for using (5) is met when operating on the degree of coherence from (2). Furthermore, the cdf for the coherence estimate as a function of true coherence γ and number of independent samples M, $P(\hat{\gamma}|\gamma, M)$, is available in [38]. We can also express the cdf of the maximum over multiple lags, which can be used with (4) and (5) to provide the expected bias on the coherence of the cross-correlation estimate.

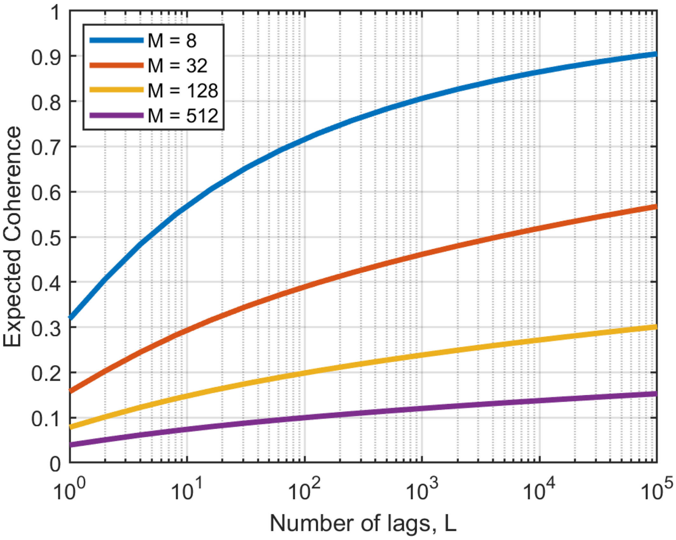

Fig. 3. Effective coherence floor of the cross-correlation estimator for different number of independent samples M and number of lags L evaluated, using a sliding window cross-correlation.

2) Coherence Floor: For the case of $\gamma = 0$, the true coherence is zero for any lag, such that the maximum over L lags at critical sampling corresponds to the maximum over L independent samples from $P(\hat{\gamma}|\gamma = 0, M)$. The cdf for the maximum of L independent samples $P_{\max}(\hat{x}, L)$ taken from a distribution with cdf $P_x(\hat{x})$ is [39, p. 92]

$$P_{\max}(\hat{x}, L) = P_x(\hat{x})^L. \tag{6}$$

Thus, for $\gamma = 0$, we can use $P(\hat{\gamma}|\gamma, M)$ from [38] with (5) and (6) to predict the estimated coherence from a sliding window cross-correlation

$$\hat{\gamma}(\gamma = 0, M, L) = \int_0^1 \left(1 - P(\hat{\gamma}|0, M)^L\right) d\hat{\gamma}. \tag{7}$$

The coherence estimate has its lowest expectation value for $\gamma = 0$, where only the bias contributes, and we denote this minimum the coherence floor. To illustrate the impact of the bias, we evaluate the coherence floor for different numbers of independent samples M and lags L, and present the results in Fig. 3. We observe that to keep the coherence floor at a minimum, the search of the cross correlation should use long time series and cover a minimum number of lags. The latter can be achieved by exploiting any *a priori* information on the expected lags.

III. SPECKLE DECORRELATION

In this section, we evaluate the theoretical limit on the spatial coherence from the van Cittert–Zernike theorem, and we derive simplified formulas for the maximum feasible along-track and range baselines.

A. The Van Cittert–Zernike Theorem

A speckle pattern originates from the superimposed backscattering of all scatterers within each resolution cell. If the relative distance to the individual scatterers changes, the speckle pattern also changes.

The van Cittert–Zernike theorem, developed in the field of statistical optics, relates the spatial coherence of the field measured at two points to the spatial intensity distribution of an incoherent source [27, Ch. 10.4.2]. The theorem cannot be applied directly to coherent acoustic sources, though it can be applied to the incoherent acoustic field scattered off a speckle scene, treating this as an incoherent source [29]. The pressure field $H_i(\vec{p})$ at seafloor position $\vec{p}$ and originating from transducer i can be estimated by integrating the contributions from all positions $\vec{s}$ on the front surface of the transducer. With $O_i(\vec{s})$ representing the aperture function of transducer i, the pressure field becomes

$$H_i(\vec{p}) = \iint_{\text{transducer}} O_i(\vec{s}) \frac{e^{jkr_i}}{r_i} dS \tag{8}$$

where $r_i = |\vec{p} - \vec{s}|$ and $k = 2\pi/\lambda$ is the acoustic wave number at wavelength λ. The scattered field follows as the product of the pressure field and the scattering function. Assuming an unresolvable, randomly distributed microstructure, the autocorrelation of the scattering function is nonzero for zero spatial lag only, where it returns the scattering amplitude χ_0 of the medium. Thus, the spatial covariance Γ_{12} between the two transducers at their separate positions follows from the van Cittert–Zernike theorem as

$$\Gamma_{12} = \chi_0 \iiint_{\text{scene}} \frac{H_1 H_2^*}{r_1 r_2} e^{jk(r_2 - r_1)} dV \tag{9}$$

where we have assumed that χ_0 is representative over the scene. The spatial coherence follows by normalization

$$\gamma_{12} = \Gamma_{12} / \sqrt{\Gamma_{11}\Gamma_{22}}. \tag{10}$$

While the van Cittert–Zernike theorem propagates the spatial correlation in 3-D, it is perhaps most known for describing a 2-D Fourier relation orthogonal to the look direction between the spatial coherence and the spatial intensity distribution of an incoherent source. This Fourier relation applies as long as both the dimensions of the source and the distance between the observations are small compared to the distance to the source [27, Ch. 10.4.2]. With pulse echo measurements, the scattered field from a speckle scene can be treated as a distributed incoherent source [29]. We note that there is a 2-D Fourier relation also between the aperture function and the scattered field in the far-field region [40, Ch. 4.3]. The spatial coherence (orthogonal to the look direction) from the combined use of multiple apertures is given by the product of the spatial coherence of each aperture. From the Fourier relations, it follows that the spatial coherence orthogonal to the look direction can be obtained directly from a normalized convolution of the individual aperture functions.

B. Numerical Evaluation

To establish the correlation function for along-track and range baselines between two single ping SAS measurements, we have performed a numerical evaluation of the van Cittert–Zernike theorem.

The spatial covariance of (9) is separable on range and the cross-range coordinates [29], such that for short patch lengths l, the spatial coherence can be estimated through an evaluation at a single range. We simplify this evaluation by adopting a flat seafloor and by positioning the transducers in the seafloor plane. Switching to a polar coordinate system (r_1, α_1) with transducer 1 at the origin and facing $\alpha_1 = 0$, the Jacobian becomes r_1, and the integral of (9) can be reduced to

$$\Gamma_{12}(r_1) \approx l\chi_0 \int_{-\pi/2}^{\pi/2} \frac{H_1 {H_2}^*}{r_2} e^{jk(r_2 - r_1)} d\alpha_1. \tag{11}$$

In our numerical evaluation, we computed H_i over a fine Cartesian 2-D grid, using a transmitter element of length $d = 2.5\lambda$, corresponding to a –3-dB beamwidth of 23°, and using a different number, $N<$ of combined receiver elements for reception. We windowed H_1 around a patch range of $r_1 = 100\,\text{m}$, and convolved this range-tapered H_1 with H_2 to estimate the covariance from (11) as a function of along-track and across-track baselines. We present the resulting predictions of the coherence $\hat{\gamma}$ in Fig. 4, where we have normalized the baselines on the element length d and wavelength λ.

For the along-track baseline, the spatial coherence could also have been obtained from the autocorrelation of the combined transmitter–receiver aperture function. If either transmitter or receiver is small, the shape should approximate a triangle, and with transmitters and receivers of equal length, the shape should approach a Gaussian [29], [31]. This is in line with our results in Fig. 4 for, respectively, long and short effective receiver elements.

For the range baseline, we have been unable to find any published results. Our numeric evaluation shows that for baselines larger than δ^2/λ, similar to the nearfield–farfield crossover [41], the coherence decays exponentially with the baseline. For shorter baselines, the coherence decays more weakly with baseline. The different decays of the two regions are consistent with different processes dominating at either side of the nearfield–farfield crossover. In both regions, the decorrelation is slower for large apertures or small wavelengths.

C. Critical Baseline and Decorrelation Baseline

The *critical baseline* is the minimum baseline Δ for which two observations decorrelate completely, and we denote this $\Delta_{\gamma=0}$. The expression is commonly used as a compact representation of decorrelation from stretching, caused by a relative change of grazing angle, which is assumed to decay linearly with the baseline. To relate the impact of contributions to decorrelation with nonlinear decay, including the across-track decorrelation that only asymptotically approaches zero, we choose to consider the baseline where the coherence between two observations is 0.5, $\Delta_{\gamma=0.5}$, and we define this the *decorrelation baseline*.

D. Predicted Decorrelation Baseline at Far Range

We develop an approximate expression for the decorrelation baseline of coherence 0.5 at far range. We simplify the task by

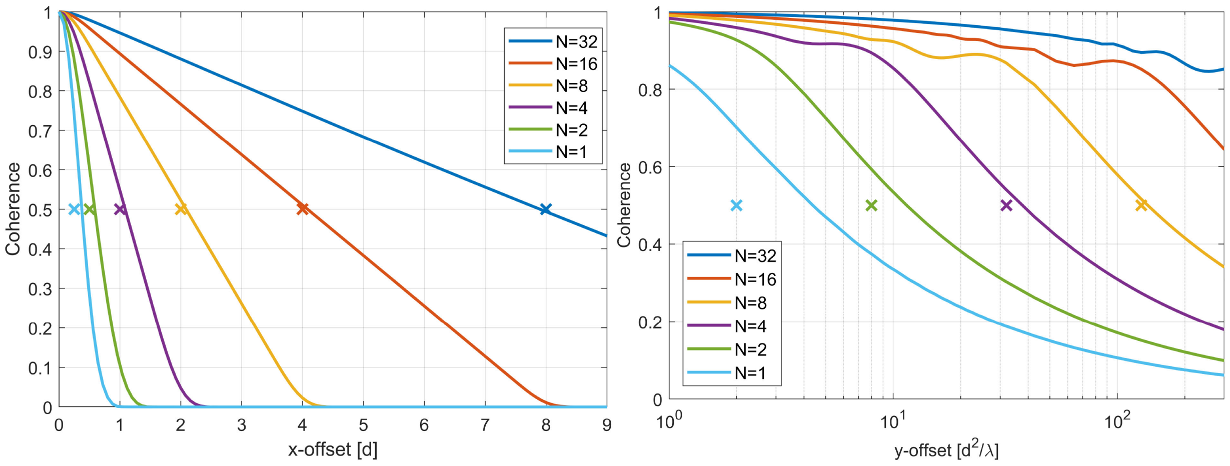

(a)

(b)

Fig. 4. Baseline decorrelation for SAS systems as predicted from the van Cittert–Zernike theorem, shown as solid lines. For simplicity, we have assumed equally sized transmitter- and receiver-elements and an in-plane seafloor, and results for combining multiple receiver elements N into larger effective elements are displayed in the labeled colors. The decorrelation baseline of coherence 0.5 from our simplified formulas of (15) and (16) for effective element length of $\delta_{\text{eval}} = Nd$ is included as crosses (x). The evaluation has been executed for a patch range of 100 m, a wavelength of $\lambda = 1.5$ cm, and an element length of $d = 2.5\lambda$, resulting in an element beamwidth of 23°. (a) Along-track baseline decorrelation. (b) Across-track baseline decorrelation.

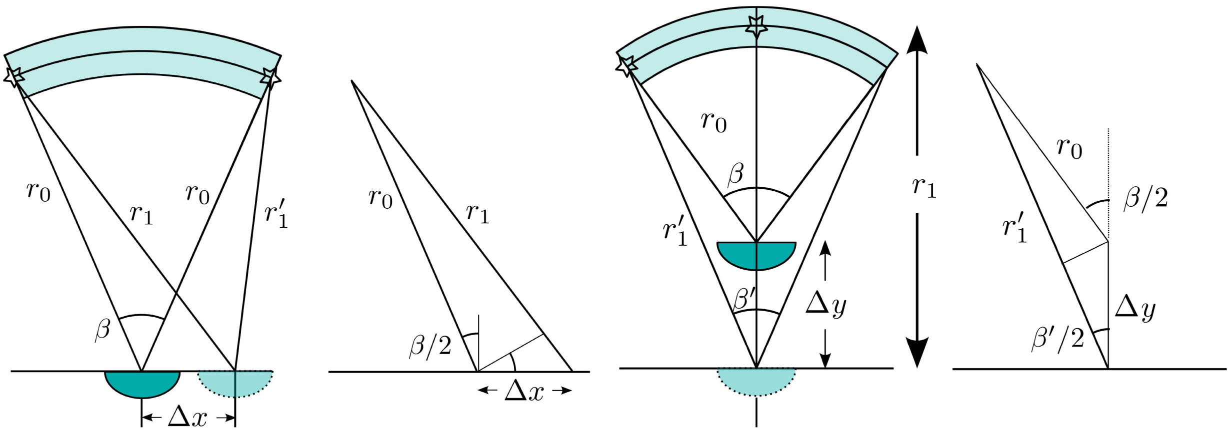

(a)

(b)

Fig. 5. Baseline decorrelation on a speckle scene follows from the relative change of the traveled distance, $\Delta r = |\Delta r_0 - \Delta r_1|$, within the sensor footprint as a function of along-track baseline Δx and across-track baseline Δy. The beamwidth is β and the stars indicate the location of the scatterers with the maximum relative change of the traveled distance for each geometry. (a) Along-track baseline decorrelation. (b) Across-track baseline decorrelation.

addressing only the two scatterers within the -3-dB beamwidth that encounter the maximum relative phaseshift with changed along-track and range baselines, as illustrated in Fig. 5. We hypothesize that the baseline that changes the two-way traveled distance over the -3-dB beamwidth β by one wavelength corresponds to the decorrelation baseline of coherence 0.5. We have validated our results on the along-track and across-track baselines through a comparison with both the numerical evaluations of Section III-B, and to already published experimental results.

We let r_0 denote the one-way traveled distances between the original sensor position and either scatterer, and for shifted sensor positions, we use the notation r_1 and r_1', to obtain the relative change of the one-way traveled distance between the two scatterers

$$\Delta r = (r_1 - r_0) - (r_1' - r_0) = r_1 - r_1'. \tag{12}$$

For the along-track offset $\Delta x \ll r_0$ in Fig. 5(a), we obtain

$$\Delta r(\Delta x) \approx 2(r_1 - r_0) \approx 2\Delta x \sin(\beta/2). \tag{13}$$

The relative change of the one-way traveled distance between the two scatterers in Fig. 5(b) for an across-track offset $\Delta y \ll r_0$ is

$$\Delta r(\Delta y) = \; r_1 - r_1' \approx \Delta y - \Delta y \cos(\beta/2). \tag{14}$$

We insert for the relative two-way distance of one wavelength, $2\Delta r = \lambda$ in (13) and (14), and assume a linear array of effective length $\delta > \lambda$, such that we can approximate $\sin \beta/2 \approx \lambda/2\delta$ and

$\cos(\beta/2) \approx 1 - (\beta^2/8)$. Thereby, we predict the decorrelation baselines

$$\Delta x_{\gamma=0.5} \approx \frac{\delta}{4} \tag{15}$$

$$\Delta y_{\gamma=0.5} \approx \frac{2\delta^2}{\lambda} = \frac{2d}{\beta} \tag{16}$$

valid for baselines $\Delta x \ll r_0$ and $\Delta y \ll r_0$. Here, δ is an effective element length with -3-dB beamwidth matching that of the combined transmitter and receiver beampatterns. Where either transmitter or receiver is long and the other short, the effective array length is roughly the length of the longest, such that for using a receiver of N times the length of the transmitter length d, we approach $\delta = Nd$ for large N. Where both transmitter and receiver are of equal length, the effective element length is $\delta = \sqrt{2}d$ [42, App. A].

We have validated the along-track decorrelation baseline predicted from using (15) with $\delta = Nd$ by comparing with the experimental results for $N = 16$ and $N = 31$ from [29]. While we have moved both transmitter and receiver (to represent correlation between SAS pings), they only moved the receiver. Thus, their result of twice our predicted baselines is consistent with the expectations, as they only experience half our change of the traveled distance.

We also indicate our predicted decorrelation baselines of (15) and (16) for effective element lengths of $\delta_{\text{eval}} = Nd$ and $r_0 = 100$ m, by crosses in Fig. 4. This allows for comparison with the along-track and across-track baseline decorrelation from our evaluation of the van Cittert–Zernike theorem in Section III-B. We observe that for large N, both the along-track decorrelation baseline of (15) and the across-track decorrelation baseline of (16) are in line with our evaluation of the van Cittert–Zernike theorem. For smaller N, there is an increasing discrepancy, but we observe that for $N = 1$, this error matches the approximation error of $\delta_{\text{eval}} = \delta_{\text{true}}/\sqrt{2}$ and δ_{eval}^2 for the along-track and across-track decorrelation baselines, respectively. This indicates that our expressions for these decorrelation baseline are quite accurate.

E. Predicted Decorrelation Baseline at Near Range

We recognize that the requirements of $\Delta x \ll r_0$ and $\Delta y \ll r_0$ for the validity of (15) and (16) roughly correspond to matching beamwidths and ranges of the two observations. This requirement is typically met for the along-track baseline Δx, as the minimum practical operation ranges for synthetic aperture systems is a huge number of element lengths, and even many physical array lengths. However, for the across-track baseline, the requirement is challenged for long effective baselines and/or short wavelengths. Therefore, we revisit the derivation of speckle decorrelation with across-track baseline for this domain. We stress that this derivation only addresses decorrelation within the overlapping footprints while the effect of decorrelation from the footprint mismatch with across-track baseline is treated separately in Section IV-B.

The relative change Δr of the one-way traveled distance between the two scatterers in Fig. 5(b) can be expressed as a function of the across-track offset Δy from inserting the relation $r_1 = r_0 + \Delta y$ into (12) to provide

$$\Delta r = r_0 + \Delta y - r_1'. \tag{17}$$

The unknown r_1' can be obtained by applying the law of cosines in Fig. 5(b) to give

$$r_1'^2 = r_0^2 + \Delta y^2 + 2r_0 \Delta y \cos(\beta/2). \tag{18}$$

We can now obtain $r_1'^2$ both from (17) and (18) and solve the equations for Δy. To estimate the decorrelation baseline of coherence 0.5, again we insert for the relative two-way distance of one wavelength, $2\Delta r = \lambda$, and assume a linear array of effective length $\delta > \lambda$, such that we can approximate $\cos(\beta/2) \approx 1 - (\beta^2/8)$, where $\beta = \lambda/\delta$. Then, we reach an expression for the across-track decorrelation baseline from curvature mismatch

$$\Delta y_{\gamma=0.5} = \frac{1 - \frac{\lambda}{4r_0}}{\frac{\lambda}{4\delta^2} - \frac{1}{r_0}} \approx \left(\frac{\lambda}{4\delta^2} - \frac{1}{r_0}\right)^{-1} \tag{19}$$

where the approximation is valid for the general case of $r_0 \gg \lambda/4$. We may rewrite (19) as a scaling of the far-range decorrelation baseline $\Delta y_\infty = 4\delta^2/\lambda$ of coherence 0.5 from (16) to give

$$\Delta y_{\gamma=0.5}(r_0) = \Delta y_\infty \left(1 - \Delta y_\infty / r_0\right)^{-1}. \tag{20}$$

Here, r_0 represents the shortest of the two ranges, such that $\Delta y > 0$. Thus, the near range extension of (16) through (19) and (20) is applicable for any $r_0 > \Delta y_\infty$, whereas for ranges $r_0 < \Delta y_\infty$, the coherence is always above 0.5.

We recall that the speckle decorrelation of (20) is evaluated over the overlapping footprint only. Therefore, it is always accompanied by the decorrelation from footprint mismatch with an along-track baseline, addressed in Section IV-B. Comparing the two shows that speckle decorrelation has the shortest decorrelation baseline of the two contributions only for ranges $r_0 < 2\Delta y_\infty$.

IV. FOOTPRINT MISMATCH

In this section, we investigate decorrelation from a footprint mismatch between observations and, specifically, its effect in change of scene illumination after accounting for any difference in time delay. We note that the related term of *footprint shift* is typically used for the offset before delay compensation [35]. Here, we focus on the change of azimuth look direction, causing an azimuth mismatch between the sensor footprints, and on changes of across-track or vertical distance, causing changes of the sector span of the footprint. We note that changes of the footprint illumination with recording geometry can be reduced and potentially mitigated if the beam can be steered and the beamwidth altered to compensate for any changes induced by the recording geometry. This can be done in postprocessing for the case of combining multiple elements before crosscorrelating.

A. Azimuth Look Direction

The decorrelation with the change of azimuth look direction $\Delta\alpha$ has been investigated in [24]. The coherence was found to fall linearly with $|\Delta\alpha|$ and pass the coherence of 0.5 at an azimuth look direction of

$$|\Delta\alpha|_{\gamma=0.5} \approx \frac{\beta}{2\cos\varphi} \tag{21}$$

where φ is the grazing angle on the seafloor. The result applies to a sinc azimuth beampattern and can, thus, be adopted for linear arrays with -3-dB beamwidth $\beta < \cos\varphi$.

B. Across-Track Baseline

The decorrelation from footprint mismatch with across-track baseline can be related to the overlapping sector lengths in Fig. 5(b). By adopting the simplified beampattern from Section III-D with unity intensity within the -3-dB beamwidth and zero outside, the coherence follows from the radial overlap

$$\gamma_{\text{rad}} = \frac{\beta'}{\beta} \approx \frac{r_0}{r_1'} \approx \left(1 + \frac{\Delta y}{r_0}\right)^{-1} \tag{22}$$

where we have inserted r_1' from (17) and approximated $\beta \ll 1$ and $\Delta y \gg \Delta r$. We solve for Δy and obtain

$$\Delta y \approx r_0 \left(\frac{1}{\gamma_{\text{rad}}} - 1\right). \tag{23}$$

Therefore, the across-track decorrelation baseline of coherence 0.5 from across-track baseline footprint mismatch is $\Delta y \approx r_0$.

C. Altitude

A sensor with -3-dB beamwidth β has a footprint of length $l = r\beta$ when the sensor is located at the ground level. From the derivation of (21), we deduce that an elevated sensor, observing the ground with a grazing angle φ, will have a footprint of length

$$l(\beta, \varphi) \approx \frac{r\beta}{\cos\varphi} \tag{24}$$

for $\beta < \cos\varphi$. By adopting a simple model of the beampattern with unity amplitude within the -3-dB width and zero outside, we estimate that a change of grazing angle will give a decorrelation from the related footprint mismatch of

$$\gamma \approx \frac{l(\beta, \varphi_{\min})}{l(\beta, \varphi_{\max})} = \frac{\cos\varphi_{\max}}{\cos\varphi_{\min}}. \tag{25}$$

We evaluate the decorrelation baseline of coherence 0.5 from (25), and find that the resulting change of grazing angle roughly can be numerically approximated by

$$\Delta\varphi_{\gamma=0.5} \approx \frac{1}{3}(\pi - 2\varphi_{\min}). \tag{26}$$

V. STRETCHING

In this section, we investigate decorrelation from a change of grazing angle, through examining the related relative stretching of the ground range sampling. Our contribution is to relate the stretching to decorrelation, and to develop a formula for the decorrelation baseline. We conclude the section by examining candidate approaches for stretch compensation, which can be used to reduce or sometimes even mitigate decorrelation from the change of grazing angle.

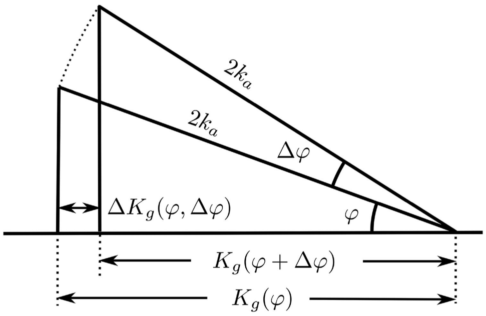

Fig. 6. Acoustic signal of wave number k_a maps the seafloor scattering at different ground wave numbers K_g at seafloor grazing angles φ and $\varphi + \Delta\varphi$.

A. Change of Grazing Angle

Observations of the seafloor with different grazing angles measure different spectral components of the seafloor scattering. This results in a decorrelation caused by a combination of wave number mismatch and stretching of the data within the overlapping wave numbers [24], [32]–[34]. The decorrelation from stretching within the overlapping wave numbers can be reduced or even mitigated if the stretching is accurately estimated and compensated for. The limitations by volume or out-of-plane contribution has been studied in [33] and [34]. The decorrelation from wave number mismatch can be avoided either by changing the measurement frequency, or at the cost of reduced range-resolution by bandpass filtering the overlapping ground wave numbers, under the assumption that there is some overlap [34], [43].

The wave number shift for small relative bandwidth and homogeneously sloping ground was estimated and compensated for in [34]. This approach was extended to large relative bandwidths by including wave number stretching and destretching in [35]. Here, we use a ground wave number interpretation to reach their expression on stretching as a function of a change of grazing angle.

Consider an acoustic signal interacting with the seafloor at grazing angle φ, which maps the seafloor scattering at ground wave number

$$K_g(\varphi) = 2k_a \cos\varphi \tag{27}$$

where the acoustic wave number is $k_a = 2\pi f/c = 2\pi/\lambda$. If the grazing angle is increased by $\Delta\varphi$, the same acoustic signal will map a smaller ground range wave number

$$K_g(\varphi + \Delta\varphi) = 2k_a \cos(\varphi + \Delta\varphi) \tag{28}$$

reflecting that the seafloor is sampled more sparsely, and is illustrated in Fig. 6. Following the work in [35], we obtain the scaling factor $\chi \in \langle 0, 1]$ (or inverse stretching factor) from the ratio of (28) to (27), and can derive

$$\begin{aligned}\chi(\varphi, \Delta\varphi) &= \frac{K_g(\varphi + \Delta\varphi)}{K_g(\varphi)} = 1 - \frac{\Delta K_g(\varphi, \Delta\varphi)}{K_g(\varphi)} \\ &= \frac{\cos(\varphi + \Delta\varphi)}{\cos(\varphi)} \approx 1 - \Delta\varphi \tan(\varphi)\end{aligned} \tag{29}$$

where the approximation is valid for a small change of grazing angle, where $\cos(\Delta\varphi) \approx 1$ and $\sin(\Delta\varphi) \approx \Delta\varphi$.

B. Ground Wave Number Mismatch

Vertical baseline and bottom slope can give a reduction of ground range wave number overlap between two observations. We quantify this decorrelation through the critical baseline. When the change of grazing angle between two observations results in a relative reduction of ground wave number that matches the ratio of bandwidth B to maximum frequency $f_{\max}$, there is no common information between the two observations, and we have reached the critical baseline (represented by the change of angle $\Delta\varphi_{\gamma=0}$)

$$\frac{\Delta K_g(\varphi, \Delta\varphi_{\gamma=0})}{K_g(\varphi)} = \frac{B}{f_{\max}} = \eta. \tag{30}$$

We choose to denote η the bandwidth relative to the maximum frequency. Generally, η differs from both fractional and relative bandwidth as defined in [44, p. 2], but we find that it provides the most compact and easily interpretable expressions in our following derivations. We recognize the relative change of ground wave number from (29), and readily obtain

$$\Delta\varphi_{\gamma=0} \approx \frac{\eta}{\tan(\varphi)} \tag{31}$$

valid for $\varphi \gg \eta$. The equations yield the same result as in [34], but without the narrowband approximation of $\eta \approx B/f_c$. For smaller baselines $\Delta\varphi < \Delta\varphi_{\gamma=0}$, it follows that the coherence is proportional to the fractional wave number overlap

$$\hat{\gamma} \approx 1 - \frac{\Delta\varphi}{\Delta\varphi_{\gamma=0}}. \tag{32}$$

The overlapping part of the spectra can be isolated through bandpass filtering, either using a fixed filter over a range interval of choice [34], [35], or using range-dependent filtering [43]. This bandpassed part of the signals will have full wave number overlap and, thus, no decorrelation, though at the cost of degraded resolution.

C. Stretch Within Overlapping Wave Numbers

We now quantify the decorrelation as a function of uncompensated stretch. Changing the grazing angle between two observations results in decorrelation also within the overlapping ground wave numbers. This decorrelation is caused by the different sample spacing–or stretching–between different angles of observation. Therefore, the decorrelation can be reduced and potentially mitigated by projecting the data onto a common frame of reference, and will be examined in Section V-D. In this section, we quantify the decorrelation from stretching within the overlapping wave numbers (as if left uncompensated).

The analytic expression for decorrelation as a function of stretching has been derived for a Gaussian weighted spectrum in [45]. For a SAS, a bandpass signal with flat spectrum might be more representative, and we adopt a numerical estimate of the coherence expectation value as a function of the applied stretching factor $1/\chi$. We evaluate (2) for $\tau = 0$ with $a_2(t) = a_1(\chi t)$ for signals $a_1(t)$ of different bandwidth and center frequency. After normalizing on both the bandwidth relative to the maximum frequency η and on the theoretical resolution δt, we obtain the general result presented in Fig. 7. The normalization on $\eta\delta t$ can be reduced to $f_{\max}$, but for the applications of this study, we find that the former can provide more insight.

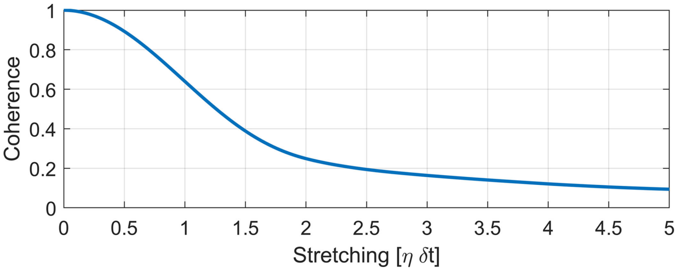

Fig. 7. Decorrelation as a function of applied stretching out from a fixed end. The plot is normalized on the bandwidth relative to the maximum frequency η and the theoretical resolution (or Nyquist sample rate) δt.

We let coherence 0.5 indicate the point of impact for decorrelation from stretching, and from Fig. 7, we observe that this occurs for a stretching of 1.25η independent samples out from a fixed end. When stretching both ends as for our case of transmit–receive, the coherence of 0.5, thus, occurs for a one-way stretching of 0.63η samples. This gives a scaling factor of $\chi_{\gamma=0.5} \approx 1 - 0.63\,\eta\,/M$, where M is the number of independent samples. We obtain the corresponding grazing angle by insertion into (29)

$$\Delta\varphi_{\gamma=0.5} \approx \frac{0.63}{M}\frac{\eta}{\tan(\varphi)} \approx \frac{0.63}{M}\Delta\varphi_{\gamma=0} \tag{33}$$

valid for $\varphi \gg \eta/M$. We observe that the baseline for coherence 0.5 from stretching is $0.63/M$ times the critical baseline of ground wave number mismatch.

D. Improving Coherence by Compensating for Stretch

The decorrelation from stretching can be reduced and ideally mitigated over the region of overlapping wave numbers if the stretch between observations is estimated and compensated for. There are at least three candidate approaches to such a compensation, which can be applied depending on which information is available.

1) Common Terrain Model and Known Baseline: This is typically the case for SAR, when accurate track navigation and digital terrain models are common. This information allows for estimating and compensating for the wave number shift or stretching encountered for narrowband systems and wideband systems, respectively [34], [35].

2) Individual Terrain Models and Unknown Baseline: This is typically the case with interferometric SAS, which allows for generation of a terrain model based on each pass [37]. For this case, the slant-range data can be mapped onto the ground and, thereby, express the local ground wave number [35]. To search for the horizontal baseline through

TABLE I
PREDICTED DECORRELATION BASELINES OF COHERENCE 0.5

Source	**Component**	**Baseline**	**Assumption**
Speckle Decorrelation	Along-track	$\Delta x \approx \frac{\delta}{4}$	$r_{\min} \gg \Delta x$
Speckle Decorrelation	Across-track	$\Delta y_\infty \approx \frac{2\delta^2}{\lambda}$	$r_{\min} \gg \Delta y_\infty$
Speckle Decorrelation	Across-track	$\Delta y \approx \Delta y_\infty \left(1 - \frac{\Delta y_\infty}{r_{\min}}\right)^{-1}$	$r_{\min} > \Delta y_\infty$
Wave Number Mismatch	Grazing Angle	$\Delta\varphi \approx \frac{1}{2}\frac{\eta}{\tan(\varphi)}$	$\varphi \gg \frac{\eta}{2}$
Wave Number Stretching	Grazing Angle	$\Delta\varphi \approx \frac{0.63}{M}\frac{\eta}{\tan(\varphi)}$	$\varphi \gg \frac{\eta}{M}$
Footprint Mismatch	Across-track	$\Delta y \approx r_{\min}$	$\beta < 1$
Footprint Mismatch	Grazing Angle	$\Delta\varphi \approx \frac{1}{3}(\pi - 2\varphi_{\min})$	$\varphi_{\min} < \cos^{-1}(\beta)$
Footprint Mismatch	Azimuth Angle	$\lvert\Delta\alpha\rvert \approx \frac{\beta}{2\cos\varphi}$	$\varphi < \cos^{-1}(\beta)$

Effective element length δ, wavelength λ, shortest range to patch $r_{\min}$, ratio of bandwidth to maximum frequency η, grazing angle on the ground φ, number of independent samples M, and -3 dB beamwidth β.

correlation, we suggest resampling the ground range data onto a grid that is equispaced horizontally, and adapting the phase such that it represents a horizontal planar propagation.

3) No Terrain Model and Unknown Baseline: This will be the case for repeated passes of a noninterferometric SAS, but the method might also be pursued for mitigating residual stretch after destretching using terrain models. For this case, a two-parameter search over baseline and stretching needs to be performed within the framework of the work in [35]. One candidate method for such a search in interferometry is [46]. We are also aware that decorrelation from stretching is a major challenge in elastography, and methods successfully countering small deformations in that field should be considered adapted to sonar [47, Ch. 5.2], [48].

VI. SUMMARY OF PREDICTED DECORRELATION BASELINES

In this section, we summarize our derived expressions on the decorrelation baseline of coherence 0.5 caused by speckle decorrelation, footprint mismatch, and stretching in Sections III–V, into Table I. Evaluated decorrelation baselines can be used to indicate the baseline of impact for the individual contributions. Because their functional dependence on the baseline differs, the relative impact of the contributions may change for other coherence values. For sources of decorrelation with near linear dependence to baseline, the baseline of zero coherence, often denoted the critical baseline, is twice the decorrelation baseline of coherence 0.5; c.f. Section III-C.

We recall that δ is the effective element length as defined in Section III-D, λ is the wavelength, β is the -3-dB beamwidth, r is the average range to the patch over two observations, with $r_{\min}$ the shortest, η is the ratio of bandwidth to maximum frequency, φ is the grazing angle on the ground, M is the number of independent samples, and α is the azimuth look angle.

VII. EXPERIMENTAL RESULTS

To validate and demonstrate our findings, we present results from a dedicated and controlled experiment in this section. In the experiment, we collected data from two trajectories, crossing at a small relative azimuth angle, thereby recording measurements from a continuous span of across-track baselines, and over a wide span of grazing angles.

A. Experiment

The experiment was conducted on June 5, 2010 using the Royal Norwegian Navy's HUGIN-MR AUV with its HISAS 1030 SAS [49]. The SAS system constitutes an interferometric SAS configuration with two vertically displaced 32 element arrays on either side. Each of the receiver elements are 0.0375 m long, and the transmitter is 50% longer. The center frequency is a 100-kHz chirp signal with a programmed bandwidth of 30 kHz. HUGIN navigates using a Doppler velocity log (DVL)-aided inertial navigation system and has a navigation drift in the order of 0.1% of the traveled distance for straight lines, and only around 0.01% of the traveled distance when revisiting a position [11]. From the same reference, we find a heading bias for the gyro compass of $0.04°$. Because HISAS is an interferometric sensor, it can also estimate the bathymetry. Therefore, the collected data should be well suited to estimate and account for the angle of incidence on the seafloor by projecting the data onto ground range, following Section V-D2.

The experiment was planned such that it collected data from repeated passes with crossings at an angle of $5°$. Because the system has a -3-dB beamwidth of $23°$, the azimuth footprint mismatch was still rather small during the data collection. In Fig. 8, we show the SAS reflectivity and bathymetry over the target scene, together with the estimated track positions. The temporal separation between the tracks was around 10 min, the AUV speed was 3.9 kn, its altitude 24 m, and the water depth 196 m. The main features that can be observed are the trawl

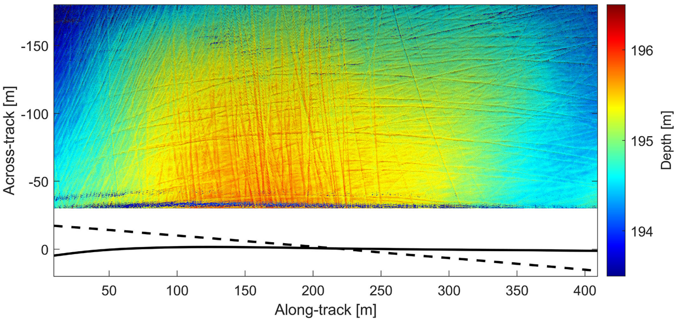

Fig. 8. SAS intensity image of the target scene, color-coded using SAS bathymetry. We observe trawl tracks on a rather flat and homogeneous seafloor. The estimated navigation of the first pass and second pass, crossing at roughly 5°, is illustrated by the solid and dotted lines.

tracks, whereas the scene appears rather flat and homogeneous otherwise.

B. Cross Correlation

We chose a patch length of 4.8 m, corresponding to around 128 independent samples with an effective signal bandwidth of 20 kHz. The rather long patch assured a low bias floor on the cross-correlation output. We selected patches from the slant-range data of the first pass at distances of 50, 100, and 150 m. For the second pass, we gathered ping data not only from the estimated closest point of approach, but also from 9.6 m of range samples and within ±3 standard deviations of the along-track navigation drift, returning data from 9 pings of 28 nonoverlapping elements each. Then, for each element position of the first pass, we correlated the patch data with the candidate patch data from the second pass using a sliding window cross-correlation. We illustrate the maximum coherence versus along-track element offset over 5 of the pings for the patch at 100-m range in the upper panel of Fig. 9 and the corresponding delay estimate in the lower panel. As with SAS micronavigation, we have estimated the slant-range baseline from the delay corresponding to the highest coherence, and the along-track offset from the location of the coherence peak. We obtained multiple estimates (of coherence and delay) per ping of the first pass, and chose to average these to reduce the variance of the estimate. We also repeated the correlation process for larger effective elements, obtained by combining neighboring elements.

C. Minimizing Decorrelation

We attempted to minimize the decorrelation from footprint mismatch and from stretching in our processing. When combining elements into larger effective elements, we steered the beam of the repeated pass to compensate for the relative change of azimuth look direction, as measured by the onboard navigation system. We also explored microsteering around these measured angles. An upper limit on the cross-track coherence is available from the interferometric coherence between the two banks when using all 32 receiver elements. This was constantly measured to above 0.98 at 100-m range.

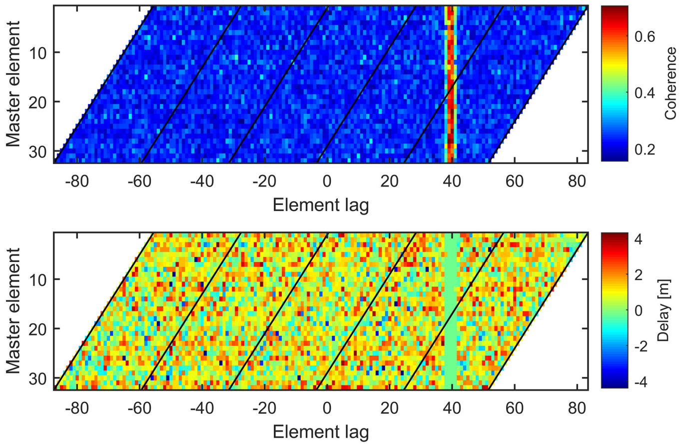

Fig. 9. Estimated coherence (upper) and delay (lower) by correlating element time series of ping 525 of the first pass with element time series for five consecutive pings of the repeated pass. Elements corresponding to the different pings of the second pass are separated by diagonal lines. The data from the first pass correspond to around 100-m slant range, and we have applied a sliding window cross-correlation of 4.8-m length, corresponding to 128 independent samples. The high coherence observed around lag 40 indicates overlapping phase centers and, thus, reflects the along-track displacement, whereas the corresponding delay reflects the across-track displacement.

We reduced the decorrelation from stretching by the following application of the method of Section V-D2: We chose a grid that was equispaced horizontally, and that followed the seafloor bathymetry $z(y_g)$. We recorded the bathymetry individually for each pass, to provide $r(y_g)$, and estimated the ground range projection $a(y_g)$ of each signal $a(r_s)$ through

$$a(y_g) = \mathcal{I}\left\{r_s, a(r_s)\cdot O(r_s), r(y_g)\right\}\cdot O^*(r(y_g)) \tag{34}$$

where $\mathcal{I}\{x, f, y\}$ denotes interpolation of $f(x)$ onto y. $O(r) = \exp\{-i2\pi f_c 2r/c\}$ is a mixing term, accounting for the phase revolution at carrier f_c as a function of range.

We illustrate the resulting coherence estimates versus estimated across-track (or sway) baseline in Fig. 10.

D. Results

In Fig. 11, we present the estimated effective coherence as a function of estimated across-track baseline for all three patches. We present results both for correlating slant-range data, and for correlating ground range data after destretching by use of (34). Smoothed and extrapolated across-track estimates from the ground range projected data at 150-m range of combining 16 receiver elements have been adopted as ground truth for the across-track baseline. This provided an estimate of the across-track baseline with subwavelength accuracy, also where the estimated coherence was low, as with shorter receiver arrays and at shorter ranges.

We have inscribed theoretical predictions of the effect of speckle decorrelation (combined with footprint mismatch) and the effect of wave number stretching into Fig. 11 for comparison. These were obtained from an evaluation of the predicted decorrelation baselines for the different sources to decorrelation with the sensor parameters and the system geometry of the experiment from Section VIII-A.

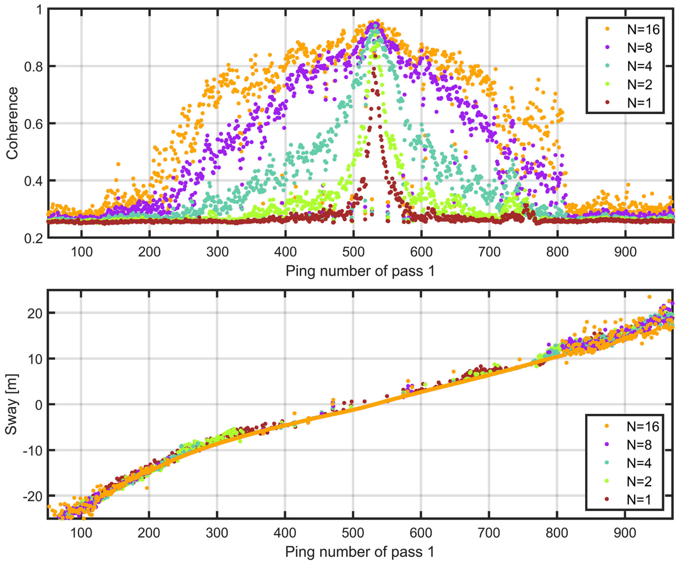

Fig. 10. Coherence and estimated sway versus ping number of the first pass for a 4.8-m patch at 150-m range with slant range to ground range conversion using the average depth.

VIII. Analysis and Discussion

We described a method for estimating the spatial coherence in Section II, before we derived decorrelation baselines of coherence 0.5 for each of the different sources of spatial decorrelation: footprint mismatch, speckle decorrelation, and stretching in Sections III, IV, and V, respectively. These formulas were assembled in Table I. Then, we reported from a controlled experiment in Section VII, where we had used an operational AUV with interferometric SAS for recording acoustic data over a continuous interval of across-track baselines. We estimated the spatial coherence on the data, and presented the results in Fig. 11, both with and without compensation for stretching.

In this section, we analyze the predicted decorrelation from using the sensor and geometry of our experiment, identify what we consider the most important sources to decorrelation in our experiment, and illustrate the predicted decorrelation from these sources in Fig. 11. Then, we analyze the experimental results supported by these predictions, before we generalize our findings.

A. Predictions

We have predicted decorrelation as a function of across-track baseline for each of the potential sources of decorrelation, by use of the formulas assembled in Table I. We have used the parameters of the experiment from Section VII to obtain the effective element lengths $\delta(N=1) \approx \sqrt{2} \times 0.0375\,\text{m}$ and $\delta(N=16) \approx 16 \times\ 0.0375\,\text{m}$ for combining N neighbor elements into larger effective elements. The wavelength $\lambda = 0.015$ m, the effective ratio of bandwidth to maximum frequency $\eta \approx 0.18$, the number of independent samples $M \approx 128$, and the -3-dB beamwidth $\beta \approx 23^\circ$. We ran the evaluation for three patches at ranges of 50, 100, and 150 m, and also included an idealized far range patch. The evaluation was executed both for correlation of single elements and for correlation of 16 receiver elements added together. We present the results in Table II, and list the evaluated patch ranges with the corresponding grazing angles in the two first rows, using italic text.

1) Correlation of Single Element Data: From Table II, we observe that for correlation of single elements, our prediction of speckle decorrelation indicates an across-track decorrelation baseline of 0.38 m for all evaluated patch ranges, thus constituting the most prominent source of decorrelation for small grazing angles. Decorrelation from stretching is predicted to give an increasing impact with larger grazing angles, and for grazing angles above 25° the decorrelation from stretching dominates, with a predicted across-track decorrelation baseline of only 0.24 m for our closest patch at 50-m range.

2) Correlation of Multiple Elements Added Together: From Table II, we observe that when processing 16 receiver elements added together, wave number stretching constitutes the most prominent source of decorrelation, with an across-track decorrelation baseline of 0.24 m at 50-m range, increasing to 7.1 m at 150-m range. If this stretching can be compensated for, the next prominent sources of decorrelation are wave number mismatch at 50-m range, limiting the decorrelation baseline to 18 m, and speckle decorrelation at far range, limiting the decorrelation baseline to 48 m.

3) Illustration of the Predictions: After making the previous observations, we have chosen to inscribe numerical estimates on the combined effect of speckle decorrelation and footprint mismatch into Fig. 11. This contribution to decorrelation was computed for the system parameters and geometry of our experiment using the method described in Section III-B. Although computed for a range of 100 m, these results should be applicable to any $r \gg \Delta y$. We also show the predicted effect of decorrelation from wave number stretching from (33) along with the results obtained without stretch compensation in Fig. 11.

B. Analysis of Experiment

We now examine the experimental results on the spatial coherence in Fig. 11 in light of our predictions on the decorrelation baseline of coherence 0.5 for an across-track baseline from Table II, and our theoretical curves inscribed into Fig. 11.

1) Azimuth Look Direction: For our experiment, the relative heading between the tracks was around 5°. We obtained a ground truth on this relative heading from the on-board INS-system, with an error that is presumed to be smaller than the absolute azimuth heading bias of 0.04° reported in Section VII-A. The predicted decorrelation baseline of coherence 0.5 from footprint mismatch caused by a change of azimuth look direction was predicted to 8° for correlation of single elements, and 0.7° for the correlation of 16 elements added together; c.f. Table II. Therefore, it is important to apply steering to avoid decorrelation from footprint mismatch and, in particular, for the case of adding elements together before correlating. In Fig. 11, we observe a measured coherence for slant-range correlation at 100-m range of up to 0.85 for the single-element case where no steering could

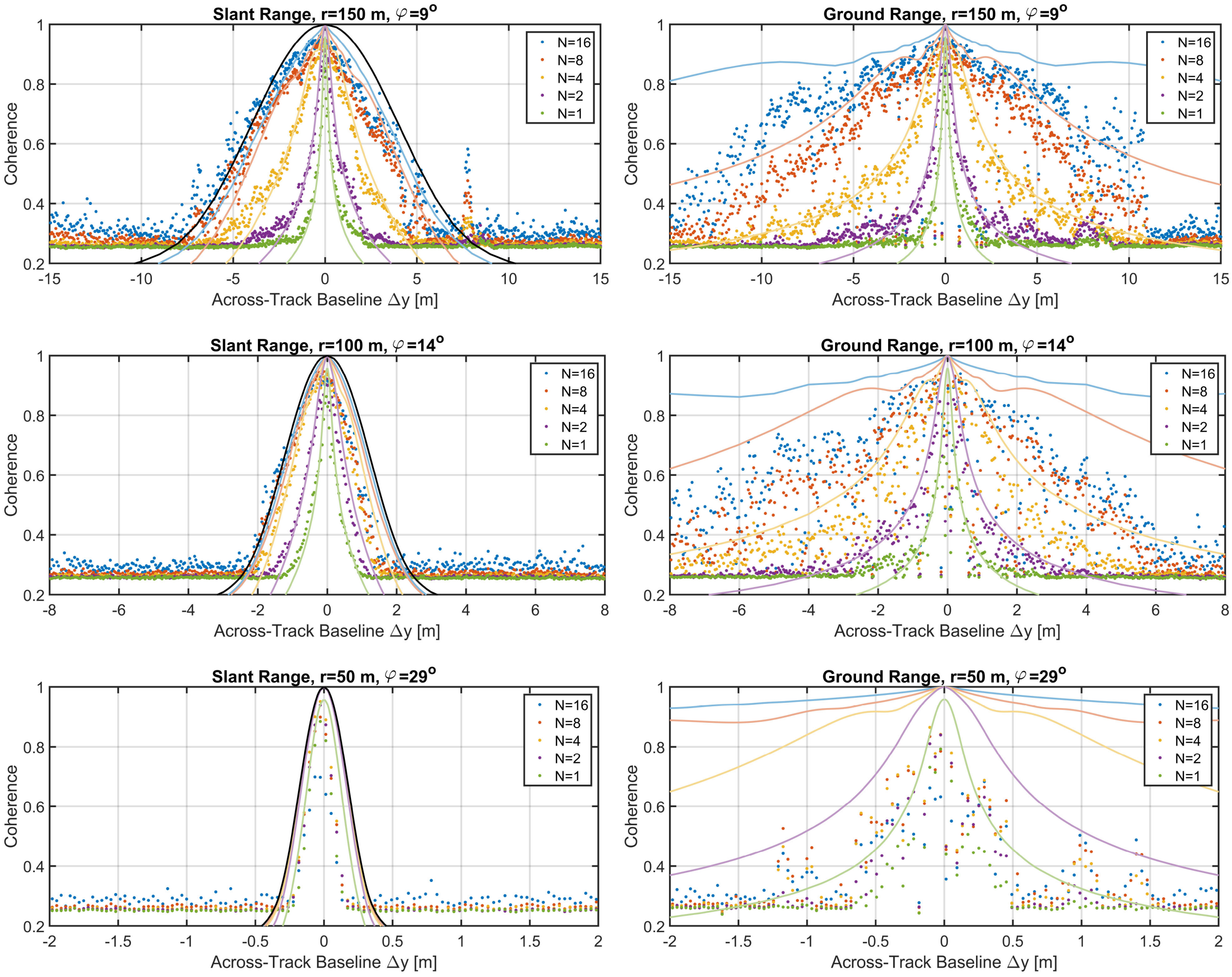

Fig. 11. Coherence between ping-pairs as a function of across-track (or sway) baseline, evaluated at slant-range distances of 50, 100, and 150 m. Left: Slant-range data. Right: Data projected onto a common ground plane. The colors indicate the number of receiver elements combined. While each dot represents one measurement from a ping-pair, our theoretical predictions are represented as solid lines. The colored lines show the combined model effects of speckle decorrelation and decorrelation from stretching. The black lines in the left panels show the effect of stretching only. The results apply to a patch length of 4.8 m and a ratio of bandwidth to maximum frequency of 0.2.

be applied. For the same corresponding cases of steered multi-element receiver arrays, the measured coherence increases to 0.95, which approaches the theoretical limit for combining two independent measurements of coherence 0.98, as $0.98^2 \approx 0.96$.

2) Coherence Floor: The experimental results on the spatial coherence presented in Fig. 11 show a coherence floor around 0.26–0.30. We recall that we correlated 128 range samples from the first pass with 256 range samples from 9 pings and 28 nonoverlapping element positions from the second pass, using a sliding window cross-correlation. This results in $L = (256 - 127) \times 9 \times (29 - N)$ coherence evaluations, when combining N neighbor elements into larger effective elements. According to Section II-F, and with N between 1 and 16, this should correspond to between 32 508 and 15 093 coherence evaluations, giving a coherence floor near 0.28. We find that the predicted and the measured levels of the coherence floor are in good agreement. Conferring Fig. 3, we note that a reduction of the patch length from 4 to 1 m, thus reducing the number of independent samples from 128 to 32, increases the coherence floor to around 0.53. Assuming that a full correlation over all combinations are run, this coherence floor would reduce the practical baseline of valid navigation updates to roughly half that of our example.

3) Correlation of Slant-Range Data: In the left panels of Fig. 11, we present experimental results of slant-range measurements without stretch compensation. These express the combined effect of speckle decorrelation, footprint mismatch, and stretching. Here, we observe an excellent agreement between our predictions and the measurements for all patches and all effective receiver element sizes.

4) Correlation of Ground Range Data: The decorrelation of the ground range projected (stretch compensated) measurements as a function of across-track baseline is presented in the right panels of Fig. 11. We observe that the estimated effective coherence follows the predictions for increasingly longer effective elements with longer range. Only for the patch at the shortest range, we observe an invariance on the element length. This can be a result of residue stretch, as this would cause a stronger decorrelation at the short range where the relative stretch between the

TABLE II
PREDICTED ACROSS-TRACK DECORRELATION BASELINES FOR HISAS 1030

Source	**Component**	**Parameter**	**Decorrelation baseline @ patch**			
Patch Range		$r_{\min}$	*50 m*	*100 m*	*150 m*	∞
Patch Grazing Angle		$\varphi_{\min}$	*29°*	*14°*	*9°*	*0°*
Speckle Decorrelation	Across-track	$\Delta y(N=1)$	0.38 m	0.38 m	0.38 m	0.38 m
Speckle Decorrelation	Across-track	$\Delta y(N=16)$	1200 m	92 m	71 m	48 m
Wave Number Mismatch	Grazing Angle	$\Delta y(\Delta\varphi)$	18 m	72 m	132 m	–
Wave Number Stretch	Grazing Angle	$\Delta y(\Delta\varphi, M=128)$	0.24 m	2.1 m	7.1 m	–
Footprint Mismatch	Across-track	Δy	50 m	100 m	150 m	–
Footprint Mismatch	Grazing Angle	$\Delta y(\Delta\varphi)$	35 m	85 m	136 m	–
Footprint Mismatch	Azimuth Angle	$\lvert\Delta\alpha(N=1)\rvert$	9.2°	8.3°	8.2°	8.1°
Footprint Mismatch	Azimuth Angle	$\lvert\Delta\alpha(N=16)\rvert$	0.8°	0.7°	0.7°	0.7°

Predicted across-track decorrelation baselines from evaluating Table I for the patch ranges and corresponding grazing angles listed in two upper rows, an operating altitude of 24 m, and the processing parameters and HISAS 1030 system parameters summarized in Section VIII-A.

patches is the largest. Origins for residue stretch could be a combination of local terrain variations and volume scattering, both plausible with our measurements.

C. General Discussion

1) Effective Element Size: For small grazing angles, speckle decorrelation with range baseline constitutes the most prominent source of decorrelation when correlating single-element data from repeated passes. For larger grazing angles (above 25° for HISAS 1030), wave number stretching dominates, and must be accounted for, before the fundamental limitation of speckle decorrelation can be met. While processing on single-element data provides the most accurate along-track navigation, the speckle decorrelation with range baseline rapidly falls when combining multiple elements into longer effective elements and synthetic apertures, as shown in Section III. Increasing the feasible across-track baseline of repeat-pass SAS micronavigation to above 0.5 m can be achieved, but only by increasing the effective aperture length or by reducing the wavelength from the value used in our experiment when using a single-element receiver.

2) Compensation for Stretching: With longer effective elements, decorrelation from relative stretching with a change of grazing angle between observations takes over as the dominating source of decorrelation. This contribution was investigated in Section V and comprises both ground wave number mismatch and stretching within overlapping wave numbers. While wave number mismatch is prominent for repeat-pass SAR interferometry, the impact of stretching increases with the number of independent range samples. In Section II, we saw that long-range patches can be exploited for lowering the coherence floor and detecting valid measurements of repeat-pass SAS micronavigation. As a result, stretching becomes the most important source of decorrelation for repeat-pass SAS micronavigation. This decorrelation can be reduced by stretch compensation, which is left as the critical processing step for extending the baseline of impact (toward that of speckle decorrelation). We find that stretch compensation appears to be one important area of further work for reducing decorrelation and extending the application of repeat-pass SAS micronavigation. Indeed, we believe that decorrelation from residue stretching remains the primary source of decorrelation of our data, also after the applied stretch compensation. As a consequence, we have not yet included the stretch compensation (or wave number alignment) with passband filtering of the overlapping wave numbers.

3) Repeat-Pass Micronavigation: In Section VII, we demonstrated increasing the feasible across-track baseline of repeat-pass SAS micronavigation to above 10 m, more than one order of magnitude up from what was reported before. We evaluated the spatial correlation of speckle, showing that with a fixed wavelength, 10-m baseline is only possible after combining at least eight elements from a typical SAS system while we combined 16 elements to meet this baseline. In Section I, we recognized that such an increased tolerance to across-track separation is needed to expand the feasibility of repeat-pass SAS micronavigation to cover applications with larger potential drift between passes.

IX. CONCLUSION

We have investigated the spatial correlation of speckle for repeat-pass SAS micronavigation, and showed that spatial decorrelation can be effectively described through the three contributions: 1) speckle decorrelation; 2) footprint mismatch; and 3) stretching. We demonstrated that their combined effect is in line with the spatial decorrelation observed in actual repeat-pass SAS micronavigation measurements. We parameterized the baseline of impact for the contributions, and analyzed their absolute and relative impact. We also demonstrated increasing the across-track baseline for acquisition of repeat-pass SAS micronavigation measurements by one order of magnitude to 10 m at the cost of reducing the along-track position accuracy. This expands the feasibility of repeat-pass SAS micronavigation to cover operations with larger drift between passes.

ACKNOWLEDGMENT

The authors would like to thank the Royal Norwegian Navy Mine Warfare Service for the permission to use data recorded with their HUGIN 1000-MR AUV. They would also like to thank Antony P. Lyons at the Center for Coastal and Ocean Mapping, University of New Hampshire, Durham, NH, USA, for valuable discussions, and also their colleagues at FFI's Underwater Robotics group for important feedback upon finalizing the manuscript. Finally, they would like to thank the anonymous reviewers for important feedback that enabled them to improve the final manuscript.

REFERENCES

[1] T. O. Sæbø and O. J. Lorentzen, "Synthetic aperture sonar images and bathymetries from the 2015 survey of the Skagerrak World War II Chemical Munitions Dump Site," Norwegian Defence Res. Establish., Kjeller, Norway, FFI-Rapport 2015/02345, Mar. 2016.

[2] A. R. Denny, T. O. Sæbø, R. E. Hansen, and R. B. Pedersen, "The use of synthetic aperture sonar to survey seafloor massive sulfide deposits," *J. Ocean Technol.*, vol. 10, no. 1, pp. 36–53, 2015.

[3] Ø. Sture, M. Ludvigsen, M. S. Scheide, and T. Thorsnes, "Recognition of cold-water corals in synthetic aperture sonar imagery," in *Proc. IEEE/OES Auton. Underwater Veh. Workshop*, Nov. 2018, pp. 1–6.

[4] A. A. Neto, G. P. Rodrigues, and I. D. Alvarenga, "Seabed mapping with HISAS sonar for decommissioning projects," *Sea Technol.*, vol. 58, pp. 15–18, Sep. 2017.

[5] Ø. Midtgaard and M. Nakjem, "Unmanned systems for stand-off underwater mine hunting," in *Proc. Underwater Defence Technol. Conf.*, Jun. 2016, pp. 1–7.

[6] V. L. Myers, D. D. Sternlicht, A. P. Lyons, and R. E. Hansen, "Automated seabed change detection using synthetic aperture sonar: Current and future directions," in *Proc. Synthetic Aperture Sonar Synthetic Aperture Radar*, vol. 36, Sep. 2014, pp. 1–10.

[7] V. Myers, I. Quidu, B. Zerr, T. O. Sæbø, and R. E. Hansen, "Synthetic aperture sonar track registration with motion compensation for coherent change detection," *IEEE J. Ocean. Eng.*, vol. 45, no. 3, pp. 1045–1062, Jul. 2020.

[8] Ø. Ødegård, R. E. Hansen, H. Singh, and T. J. Maarleveld, "Archaeological use of synthetic aperture sonar on deepwater wreck sites in Skagerrak," *J. Archaeol. Sci.*, vol. 89, pp. 1–13, Jan. 2018.

[9] H. D. Griffiths, T. A. Rafik, Z. Meng, C. F. N. Cowan, H. Shafeeu, and D. K. Anthony, "Interferometric synthetic aperture sonar for high resolution 3-D mapping of the seabed," *Proc. Inst. Elect. Eng.—Radar, Sonar, Navigat.*, vol. 144, no. 2, pp. 96–103, Apr. 1997.

[10] H. J. Callow, P. E. Hagen, R. E. Hansen, T. O. Sæbø, and R. B. Pedersen, "A new approach to high-resolution seafloor mapping," *J. Ocean Technol.*, vol. 7, no. 2, pp. 13–22, 2012.

[11] B. Jalving, K. Gade, O. K. Hagen, and K. Vestgård, "A toolbox of aiding techniques for the HUGIN AUV integrated inertial navigation system," in *Proc. MTS/IEEE OCEANS Conf.*, Sep. 2003, pp. 1–8.

[12] C. Roman and H. Singh, "A self-consistent bathymetric mapping algorithm," *J. Field Robot.*, vol. 24, no. 1, pp. 23–50, Feb. 2007.

[13] K. B. Ånonsen, O. K. Hagen, and E. Berglund, "Autonomous mapping with AUVs using relative terrain navigation," in *Proc. MTS/IEEE OCEANS Conf.*, Sep. 2017, pp. 1–7.

[14] Ø. Midtgaard, "Change detection using synthetic aperture sonar imagery with variable time intervals," in *Proc. 1st Underwater Acoust. Conf.*, Jun. 2013, pp. 713–720.

[15] V. T. Wang and M. P. Hayes, "Synthetic aperture sonar track registration using SIFT image correspondences," *IEEE J. Ocean. Eng.*, vol. 42, no. 4, pp. 901–913, Oct. 2017.

[16] A. J. Hunter, W. A. Connors, and S. Dugelay, "An operational concept for correcting navigation drift during sonar surveys of the seafloor," *IEEE J. Ocean. Eng.*, vol. 43, no. 4, pp. 913–926, Oct. 2017.

[17] A. Bellettini and M. A. Pinto, "Theoretical accuracy of synthetic aperture sonar micronavigation using a displaced phase-center antenna," *IEEE J. Ocean. Eng.*, vol. 27, no. 4, pp. 780–789, Oct. 2002.

[18] S. A. V. Synnes, H. J. Callow, T. O. Sæbø, and R. E. Hansen, "Multipass coherent processing on synthetic aperture sonar data," in *Proc. Eur. Conf. Underwater Acoust.*, Jul. 2010, pp. 1–7.

[19] A. J. Hunter and S. Dugelay, "Exploiting the coherence of seabed scattering for repeat-pass SAS micro-navigation," in *Proc. Seabed Sediment Acoust., Meas. Model.*, vol. 37, Sep. 2015, pp. 175–182.

[20] A. J. Hunter, S. Dugelay, and W. L. J. Fox, "Repeat-pass synthetic aperture sonar micronavigation using redundant phase center arrays," *IEEE J. Ocean. Eng.*, vol. 41, no. 4, pp. 820–830, Oct. 2016.

[21] C. Oliver and S. Quegan, *Understanding Synthetic Aperture Radar Images*. Norwood, MA, USA: Artech House, 1998.

[22] F. R. Dickey and J. A. Edward, "Velocity measurement using correlation sonar," in *Proc. IEEE Position Location Navigat. Symp.*, Nov. 1978, pp. 255–264.

[23] Y. Doisy, "General motion estimation from correlation sonar," *IEEE J. Ocean. Eng.*, vol. 23, no. 2, pp. 127–140, Apr. 1998.

[24] H. A. Zebker and J. Villasenor, "Decorrelation in interferometric radar echoes," *IEEE Trans. Geosci. Remote Sens.*, vol. 30, no. 5, pp. 950–959, Sep. 1992.

[25] V. Myers, I. Quidu, T. Sæbø, and R. Hansen, "Results and analysis of coherent change detection experiments using repeat-pass synthetic aperture sonar images," in *Proc. 1st Underwater Acoust. Conf.*, Jun. 2013, pp. 1–8.

[26] A. P. Lyons and D. C. Brown, "The impact of the temporal variability of seafloor roughness on synthetic aperture sonar repeat-pass interferometry," *IEEE J. Ocean. Eng.*, vol. 38, no. 1, pp. 91–97, Jan. 2013.

[27] M. Born and E. Wolf, *Principles of Optics*, 7th ed. Cambridge, U.K.: Pergamon Press, 1999.

[28] R. A. Thompson, J. M. Moran, and G. W. Swenson, "Van Cittert-Zernike theorem, spatial coherence, and scattering," in *Interferometry and Synthesis in Radio Astronomy*, M. A. Barstow, Ed., 3rd ed. Berlin, Germany: Springer, g2017, pp. 767–808. [Online]. Available: https://link.springer.com/book/10.1007/978-3-319-44431-4

[29] R. Mallart and M. Fink, "The van Cittert-Zernike theorem in pulse echo measurements," *J. Acoust. Soc. Amer.*, vol. 90, no. 5, pp. 2718–2727, Jul. 1991.

[30] R. Heremans, Y. Dupont, and M. Acheroy, "Motion compensation in high resolution synthetic aperture sonar (SAS) images," in *Proc. Adv. Sonar Technol.*, 2009, pp. 43–74.

[31] D. C. Brown, I. D. Gerg, and T. E. Blanford, "Interpolation kernels for synthetic aperture sonar along-track motion estimation," *IEEE J. Ocean. Eng.*, vol. 45, no. 4, pp. 1497–1505, Oct. 2020.

[32] F. K. Li and R. M. Goldstein, "Studies of multibaseline spaceborne interferometric synthetic aperture radars," *IEEE Trans. Geosci. Remote Sens.*, vol. 28, no. 1, pp. 88–97, Jan. 1990.

[33] E. Rodriguez and J. M. Martin, "Theory and design of interferometric synthetic aperture radars," *Proc. Inst. Elect. Eng. F, Radar Signal Process.*, vol. 139, no. 2, pp. 147–159, Apr. 1992.

[34] F. Gatelli, A. M. Guarnieri, F. Parizzi, P. Pasquali, C. Prati, and F. Rocca, "The wavenumber shift in SAR interferometry," *IEEE Trans. Geosci. Remote Sens.*, vol. 32, no. 4, pp. 855–865, Jul. 1994.

[35] P. Cervenka, "Geometric decorrelation in acoustic tools for surveying the seafloor," in *Proc. Acoust.*, 2012, pp. 2807–2813.

[36] R. E. Hansen, "Introduction to synthetic aperture sonar," in *Sonar Systems*, N. Z. Kolev, Ed. Rijeka, Croatia: Intech, Sep. 2011, ch. 1, pp. 3–28. [Online]. Available: http://www.intechopen.com/books/show/title/sonar-systems

[37] T. O. Sæbø, R. E. Hansen, and A. Hanssen, "Relative height estimation by cross-correlating ground-range synthetic aperture sonar images," *IEEE J. Ocean. Eng.*, vol. 32, no. 4, pp. 971–982, Oct. 2007.

[38] G. C. Carter, C. H. Knapp, and A. H. Nuttall, "Statistics of the estimate of the magnitude-coherence function," *IEEE Trans. Audio Electroacoust.*, vol. AU-21, no. 4, pp. 388–389, Aug. 1973.

[39] W. J. Ewens and G. R. Grant, *Statistical Methods in Bioinformatics: An Introduction*. Berlin, Germany: Springer, 2005.

[40] J. W. Goodman, *Introduction to Fourier Optics.*, Englewood, CO, USA: Roberts Company, 2005.

[41] X. Lurton, *An Introduction to Underwater Acoustics, Principles and Applications*, 2nd ed. Berlin, Germany: Springer, 2010.

[42] O. M. H. Rindal, "Software beamforming in medical ultrasound imaging—A blessing and a curse," Department of Informatics Ph.D. dissertation, Univ. Oslo, Oslo, Norway, 2019.

[43] A. Reigber, "Range dependent spectral filtering to minimize the baseline decorrelation in airborne SAR interferometry," in *Proc. Int. Geosci. Remote Sens. Symp.*, vol. 3, 1999, pp. 1721–1723.

[44] J. D. Taylor, "Ultra-wideband radar overview," in *Introduction to Ultra-Wideband Radar Systems*, J. D. Taylor, Ed. Boca Raton, FL, USA: CRC Press, 1994, ch. 1, pp. 1–10.

[45] T. Varghese and J. Ophir, "Enhancement of echo-signal correlation in elastography using temporal stretching," *IEEE Trans. Ultrason., Ferroelectr., Freq. Control*, vol. 44, no. 1, pp. 173–180, Jan. 1997.

[46] T. O. Sæbø, R. E. Hansen, H. J. Callow, and B. Kjellesvig, "Using the cross-ambiguity function for improving sidelooking sonar height estimation," in *Proc. Underwater Acoust. Meas.*, Jun. 2007, pp. 309–316.

[47] J. Ophir *et al.*, "Elastography: Ultrasonic estimation and imaging of the elastic properties of tissues," *Proc. Inst. Mech. Eng. H*, vol. 213, no. 3, pp. 203–233, Mar. 1999.

[48] S. K. Alam and J. Ophir, "Reduction of signal decorrelation from mechanical compression of tissues by temporal stretching: Applications to elastography," *Ultrasound Med. Biol.*, vol. 23, no. 1, pp. 95–105, 1997.

[49] P. E. Hagen, T. G. Fossum, and R. E. Hansen, "HISAS 1030: The next generation mine hunting sonar for AUVs," in *Proc. UDT Pacific Conf. Proc.*, Nov. 2008, pp. 1–8.

Stig Asle Vaksvik Synnes (Member, IEEE) was born in Ålesund, Norway, in 1972. He received the Cand.Scient. degree in atomic physics from the University of Bergen, Bergen, Norway, in 1997. He is currently working toward the Ph.D. degree in synthetic aperture sonar with the Department of Informatics, University of Oslo, Oslo, Norway.

Since 1998, he has been with the Norwegian Defence Research Establishment (FFI), Kjeller, Norway, where he has been working in the field of synthetic aperture sonar since 2008. He is currently a Principal Scientist with FFI. His research interests include wideband and widebeam synthetic aperture sonar, correlation-based navigation, and shallow water sonar performance.

Roy Edgar Hansen (Senior Member, IEEE) received the M.Sc. and Ph.D. degrees in physics from the University of Tromsø, Tromsø, Norway, in 1992 and 1999, respectively.

From 1992 to 2000, he was with the Norwegian research company TRIAD, working on multistatic sonar, multistatic radar, SAR, and underwater communications. Since 2000, he has been with the Norwegian Defence Research Establishment (FFI), Kjeller, Norway, working in the field of synthetic aperture sonar. He is currently a Principal Scientist with FFI. He is also an Adjunct Professor in acoustic imaging with the Department of Informatics, University of Oslo, Oslo, Norway. His research interests include synthetic aperture sonar and radar, ultrasound imaging, sonar signal processing, and array signal processing.

Torstein Olsmo Sæbø (Senior Member, IEEE) was born in Bergen, Norway, in 1977. He received the Cand.Scient (M.Sc.) degree in astrophysics from the University of Oslo, Oslo, Norway, in 2002, and the Ph.D. degree in physics from the University of Tromsø, Tromsø, Norway, in 2010, with a dissertation titled "Seafloor depth estimation by means of interferometric synthetic aperture sonar."

Since 2002, he has been with the Norwegian Defence Research Establishment (FFI), Kjeller, Norway, specializing in the field of interferometry on synthetic aperture sonar. From 2016 to 2020, he was a Research Manager for the Underwater Robotics research group with FFI. He is currently a Principal Scientist with FFI.

Dr. Sæbø is an Associate Editor for IEEE JOURNAL OF OCEANIC ENGINEERING.